Physica Medica 67 (2019) 148–154

Contents lists available at ScienceDirect

Physica Medica

journal homepage: www.elsevier.com/locate/ejmp

Original paper

A simulation study of gold nanoparticles localisation effects on radiation enhancement at the mitochondrion scale

Z. Francis[a,*], G. Montarou[b], S. Incerti[c], M. Bernal[d], S.A. Zein[e]

[a] Saint Joseph University, Faculty of Sciences, Department of Physics, Beirut, Lebanon
[b] Clermont Auvergne University, CNRS/IN2P3, Laboratoire de Physique de Clermont, F-63000 Clermont-Ferrand, France
[c] Centre d'Etudes Nucléaires de Bordeaux Gradignan, Université de Bordeaux 1, CNRS/IN2P3, CENBG, 33175 Gradignan, France
[d] Instituto de Física Gleb Wataghin, Universidade Estadual de Campinas, SP, Brazil
[e] Weill Cornell Medical College, Department of Radiology, New York, USA

ARTICLE INFO

Keywords:
GNP
Mitochondria network
GEANT4 toolkit

ABSTRACT

This paper presents a Monte-Carlo study focusing on the effects of gold nanoparticles on the energy deposition patterns produced by incident photons in the close vicinity of the mitochondrial network modeled as a tube. Spherical shaped gold nanoparticles of 30 nm diameter were placed in a micrometric ($10 \times 10 \times 10\,\mu m^3$) water phantom containing a tube of 300 nm diameter and 5 μm length. The tube represented a mitochondrial fragment and nanoparticles were distributed in the water phantom outside the tube. Photons of 120 keV were simulated using the Geant4 Livermore processes and the Geant4-DNA electron processes to account for secondary electrons collisions. The Livermore processes took into account the Auger cascade inside the gold material. A data mining algorithm was then used to analyze the energy deposition clusters inside the water phantom and the tube. A comparison was made between the results obtained for a uniform distribution of nanoparticles and a vesicle distribution model. The results including energy deposition clusters are also compared to dose enhancement ratios.

1. Introduction

Recently the observation of gold nanoparticles (GNP) radiosensitizing effects studies became increasingly focused on the explanation of underlying physical processes leading to the enhancement of ionizing radiation effects in biological media. In fact, dose enhancing agents were described in the literature since early eighties mainly reporting that injecting tissue with iodine enhances the radiation dose that is absorbed during X-rays irradiation [1–4].

This effort using iodine continues to be a topic of interest mainly for assessing any radiosensitizing effect during X-rays exposure and this includes radiation therapy and medical imaging techniques as well [5].

Although as a first assumption, the nanoparticles enhancing effects were attributed to increased photoelectric absorption by high-Z materials, this explanation failed for two reasons. The first is that clinically relevant energies are relatively high and therefore, interactions are dominated by the Compton scattering [6]. The second reason is that the dose enhancement ratio is relatively small and does not justify the observed increase in cell mortality ratios [7]. In fact, Lechtman et al. [7] compared cell survival results obtained by a simple macroscopic dose enhancement calculations based on the linear quadratic model versus their calculations based on the Local Effect Model [8] showing that macroscopic dose enhancement alone does not explain enhanced cell mortality observations.

Carter et al. [9] studied the importance of the localization of the nanoparticles and how it might affect the so observed radiosensitisation. They concluded that a high concentration of electrons and radicals is created around the nanoparticles and in order to achieve radiosensitisation these nanomaterials must be either delivered precisely to specific sites otherwise their concentration should be increased.

While most of the early studies were focused on nanoparticles effects inside of the nucleus and on nuclear DNA, recent studies started investigating these effects outside the nucleus and on mitochondria [10] since it appear today as the central executioner of apoptosis [11] and mitochondrial DNA (mtDNA) is also of vital importance for the cell [12].

The uptake and localization of nanoparticles in a cell depends mainly on their size as well as the nature of the coating. Nanoparticles with diameter less than 6 nm tend to be more penetrating and have

* Corresponding author.
E-mail address: ziad.francis@usj.edu.lb (Z. Francis).

https://doi.org/10.1016/j.ejmp.2019.10.038
Received 30 July 2019; Received in revised form 19 October 2019; Accepted 24 October 2019
Available online 07 November 2019

more chances to reach the nuclear volume. For the large diameters, exceeding 20 nm, nanoparticles are mostly located in the cytoplasm [9]. This plays a significant role on radiosensitising effect since the abundant low energy electrons created around the nanoparticle have little chance of reaching the nuclear DNA if the nanoparticle is located outside the nucleus. In the work of McMahon et al. [10] GNP of 40 nm diameter were located in the cytoplasm at the surface of elliptical mitochondrial structures distributed in the cell volume.

The surface accumulation of nanoparticles is justified by surface charge properties according to Karatas et al. [13]. Peckys and de Jonge [14] used scanning electron transmission microscopy to scan cells and image the intracellular uptake of 30 nm diameter GNP. In their results they showed that nanoparticles were clustered in groups, bound to membranes of vesicles and these vesicles accumulated together to form micrometer sized clusters after 24 h of cells incubation.

Kirkby and Ghasroddashti [15] also studied mitochondrial dose enhancement with 13 nm diameter GNP accumulated on mitochondrial surfaces. Their study was dedicated to radiation therapy applications therefore they used photon energies up to 6 MV nominal acceleration potential similar to those of clinical devices.

Therefore, according to the mentioned studies the spatial distribution and the penetration capacities of nanoparticles [16] can have an important impact on absorbed dose enhancement.

However, the uptake can vary largely depending on different parameters like the GNP size and the cell type [17]. Such information along with the nanoparticles distribution within the cell volume is still very scarce in the literature.

In this work two geometry setups were considered; one where nanoparticles are uniformly distributed in the irradiated volume and the second based on clustered distributions as in the experiments of Peckys and de Jonge [14]. The dose enhancement ratios due to the presence of GNP were determined and the energy depositions were also analyzed. The analysis of energy depositions was carried out using a clustering approach [18,19]. Results were obtained for both configurations using Monte-Carlo simulations with 120 keV photons which is an energy of interest for radiobiology studies.

2. Materials and methods

2.1. Geometry configurations

GNP were represented as gold spheres of 30 nm diameter. The simulation *World* volume was limited to a water cube of $10 \times 10 \times 10\,\mu m^3$.

A mitochondrial fragment is represented by a cylinder filled with water and placed at the center of the *World* volume. The dimensions of this *mitochondrial tube* are 300 nm diameter and 5 μm length. The diameter dimension was based on previous studies of Zein et al. [20] where a realistic geometry of mitochondrial phantom was built from a deconvolved widefield fluorescent microscopic image of the mitochondrial network of a fibroblast cell. In fact, the mean chord length of particles crossing the fibroblast mitochondrial phantom described in Zein et al. [20] is between 384 nm and 462 nm as calculated using the Monte-Carlo method. The length of our tube model was limited to 5 μm to simplify the simulation conditions. In general, considering larger volumes leads to a bigger *World* and therefore a higher number of nanoparticles in order to keep the same density, this would have a direct effect on the computing time. Therefore, we consider the described cylindrical shape as a sufficient approximation for a comparative study between the different nanoparticles distributions. Since the fluorescent imaging does not provide information about the content and densities of mitochondrial structures, water material was considered as a good approximation since it is also compatible with the Geant4-DNA simulation processes that are detailed in Section 2.2.

Nanoparticles were distributed in a random uniform pattern within the *World* volume excluding the *mitochondrial tube*.

Another configuration based on the experiments of Peckys and de Jonge [14] was considered, where nanoparticles were distributed on spherical surfaces called vesicles of 0.26 μm diameter. Each vesicle holds 57 nanoparticles and vesicles were grouped within spherical clusters of 4.6 μm diameter. Each cluster contained 152 vesicles randomly distributed within the cluster volume and during the whole volume placement procedure overlapping between nanoparticles and between vesicles was avoided.

Considering 3 clusters randomly placed in the *World* volume but outside the *mitochondrial tube* and without overlap between cluster volumes, the total concentration obtained was 26 nanoparticles per μm^3. This concentration is in agreement with the reference value of 0.7% mass concentration, or 7 mg Au/g in tumors, which is equal to the concentration achieved by Hainfeld et al. in tumors in mice [21] and also used by Sotiropoulos et al. [22] for Monte-Carlo simulations.

The source of photons is a parallel beam of circular shape with ~9 μm diameter covering the whole size of the *mitochondrial tube*. The initial position of the beam is randomly sampled on a virtual sphere of 5 μm radius centered at the *mitochondrial tube*'s center and the direction of photons is set inward toward the water tube. From another perspective one can imagine that the parallel beam is fixed and the orientation of the mitochondrial tube is varying randomly with each incident photon.

Fig. 1 shows a schematic representation of the basic setup, the arrows placed on the spherical surface represent an example of initial directions of photons generated as described. Note that the vectors are parallel and not directed towards a central point because this would lead to a conical beam converging at the center of the tube which is not realistic. In fact, maintaining a parallel beam ensures that the *mitochondrial tube* is irradiated parallelly from all directions, which is closer to reality since mitochondrial volumes are orientated randomly versus the incident parallel beam. Therefore, the simulation results represent an average on all considered irradiation angles.

Fig. 2 shows a representation of the described clusters setup showing the vesicles of nanoparticles regrouped into three different clusters. Since the distance separating the GNP clusters from the *mitochondrial tube* can affect the energy deposition pattern within the tube, clusters were placed randomly within the water cube showing different results as reported in the results section.

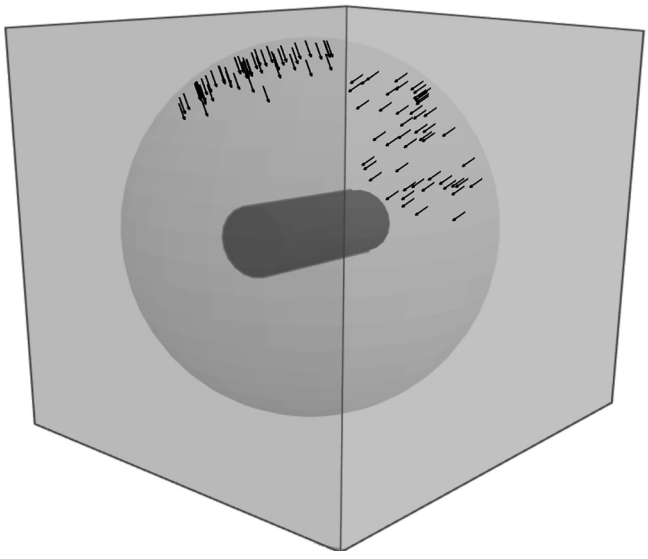

Fig. 1. Schematic representation of the irradiation geometry. The virtual sphere surrounding the tube is displayed only to indicate the possible positions of primary photons. Random beam positions are sampled on the sphere and photons are shot in a parallel direction towards the inside of the geometry. For clarity the scale and size proportions were disregarded.

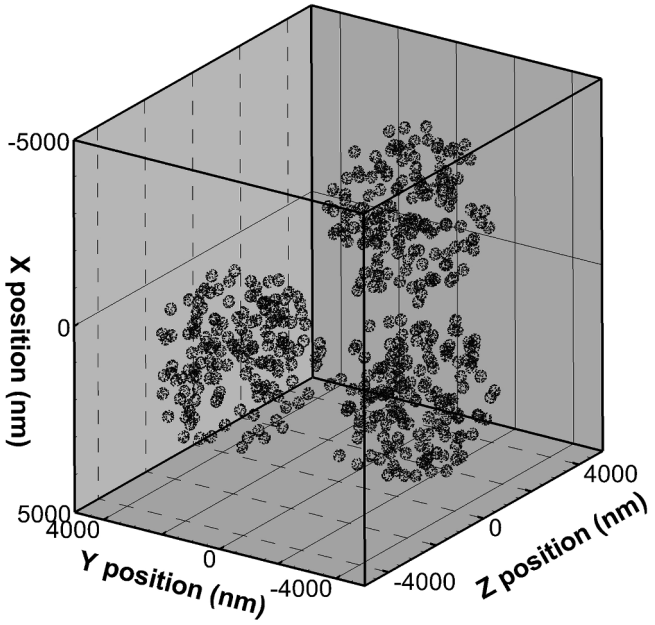

Fig. 2. GNP distribution in clusters of vesicles as described in the experiment of Peckys and de Jonge [14]. A concentration of 26 nanoparticles per μm^3 was considered which corresponds to a mass concentration of 7 mg Au/g of water in agreement with Hainfeld et al. [21]. One can distinguish 3 different clusters (4.6 μm diameter) containing the 152 spherical vesicles (0.26 μm diameter) and each vesicle contains at its surface 57 nanoparticles (30 nm diameter).

For comparison, simulations were first carried out for a water cube without the nanoparticles. After that, each of the different nanoparticles distributions was considered.

2.2. Particle tracks simulation

The simulations were carried out using the Geant4 Monte-Carlo toolkit version 10.5 [23–25]. The Livermore physics processes were used to simulate interactions of photons [26] and electrons [27] inside gold material. These processes include the photoelectric effect, the Compton and Rayleigh scattering effects for photons and elastic and inelastic collisions for electrons.

The fluorescence and Auger cascade de-excitation effects were also activated as their contribution among the Geant4 low energy processes was validated in a previous work of Incerti et al. [28] and their importance was also underlined by Xie et al.[29]. For all processes in gold, electrons production energy cut-off was set to 50 eV.

The lowest energy recommended for electrons using the Livermore libraries is 250 eV, however, it is of use within the Monte-Carlo community to stretch this limit down to lower energies, e.g. Sakata et al. [30] used a secondary production cut and lowest transport energy cut of 1 eV for simulations in gold nanoparticles. This extension is mainly used because no other practical solution is available for Monte-Carlo tracking of low energy electrons. In gold, 50 eV electrons have a range around 3.5 nm [31] almost 10 times smaller than the GNPs diameter, which allows the simulation of electrons attenuation inside the gold spheres. Electrons exiting gold spheres into the water cube were tracked using Geant4-DNA step by step processes [32–35] taking into account ionization, electronic excitation and elastic collisions. Below the energy production threshold, electrons are followed until complete stop using a continuous energy loss approach based on the linear energy transfer.

In the water volumes the cut-off energy was set to 9 eV, which means that electrons below this threshold are killed and their remaining energy is locally deposited. The vibration and rotational excitation and the electron attachment processes were not taken into account since their contribution is minimal for the considered energies above the 9 eV cut-off.

Since the lowest excitation energy for liquid water is usually around 8.22 eV [33] it is a common practice in step-by-step track structure applications to set the tracking cut-off to a value between 8 and 10 eV. Lower cut-offs, e.g., 0.025 eV, are only used when chemical species simulation is required, mainly because solvated electrons contribute largely to chemical reactions. Decreasing the cut-off would also increase computing time and so it is avoided if the chemical reactions are not considered. Our study is limited to direct interactions, therefore a value of 9 eV is a good compromise for our comparative study.

Moreover subexcitational processes can generate a huge number of steps due to the highly dominant elastic scattering process, which is heavy to consider from the computing time perspective. The importance of these low energy processes is more justified for the chemical phase which is not considered in this work. Here we assume that free radicals concentrations are directly related to the number of inelastic energy depositions. Therefore considering only the energy depositions for a comparative study should be sufficient.

2.3. Energy deposition analysis

The energy deposition points were recorded for each incident photon and their spatial distribution was analyzed using the data mining algorithm *Density Based Spatial Clustering of Application with Noise* (DBSCAN) [18]. Data mining and pattern recognition algorithms were widely used and reported in the literature for different applications including radiobiology and microdosimetry. Nikjoo et al. [36] and Pszona et al. [37] used the K-means [38] algorithm to analyze energy deposition patterns after ionizing tracks simulations. We also used DBSCAN in previous studies for protons and ions effects on biological DNA in order to estimate the simple and double strand break yields induced by irradiation [19,39,40].

As we do not intend to relate this study to DNA damages we disregarded all the parameters used in the previously published studies and related to DNA characteristics such as DNA spatial distribution, damage induction function and two strands random sampling parameter. In our case, the DBSCAN is an optimal choice since it enables us to analyze particle tracks while taking into account only two parameters which are the *minimum number of points* to form what is designated as a cluster of energy deposition points and the *maximum distance* that separates points within one cluster. This method allows us to have a nanometric scale analysis of the energy deposition patterns induced for the different irradiation conditions. The results of clustering algorithms depend largely on the user input values, on the chosen input values of the two parameters, therefore the *maximum distance* was varied from 1 nm up to 400 nm (1 nm, 50 nm, 100 nm, 200 nm, 300 nm and 400 nm) in order to analyze its impact on the obtained clusters pattern. The results of clustering were compared between the different geometry configurations and with a simulation where only water was used without nanoparticles in the water. The enhancement in the number of clusters was compared to the macroscopic dose enhancement in order to reveal the differences between macroscopic measurements and calculations on the nanometer scale.

3. Results and discussion

Simulations were carried out on a multicore I9 processor with 28 parallel threads using the multithreading feature of Geant4. The event number was about 2.4 10^9, that is the maximum technical limit in Geant4 for a single run. For our study, such a number of events is considered high enough to obtain energy deposition uncertainties below 3%. All the obtained results were then normalized per primary photon and per unit volume (μm^3).

Fig. 3 shows the energy depositions clustering results in the water box for 4 different values of the maximum distance parameter that governs the clustering:1 nm, 50 nm, 100 nm and 300 nm. The frequency

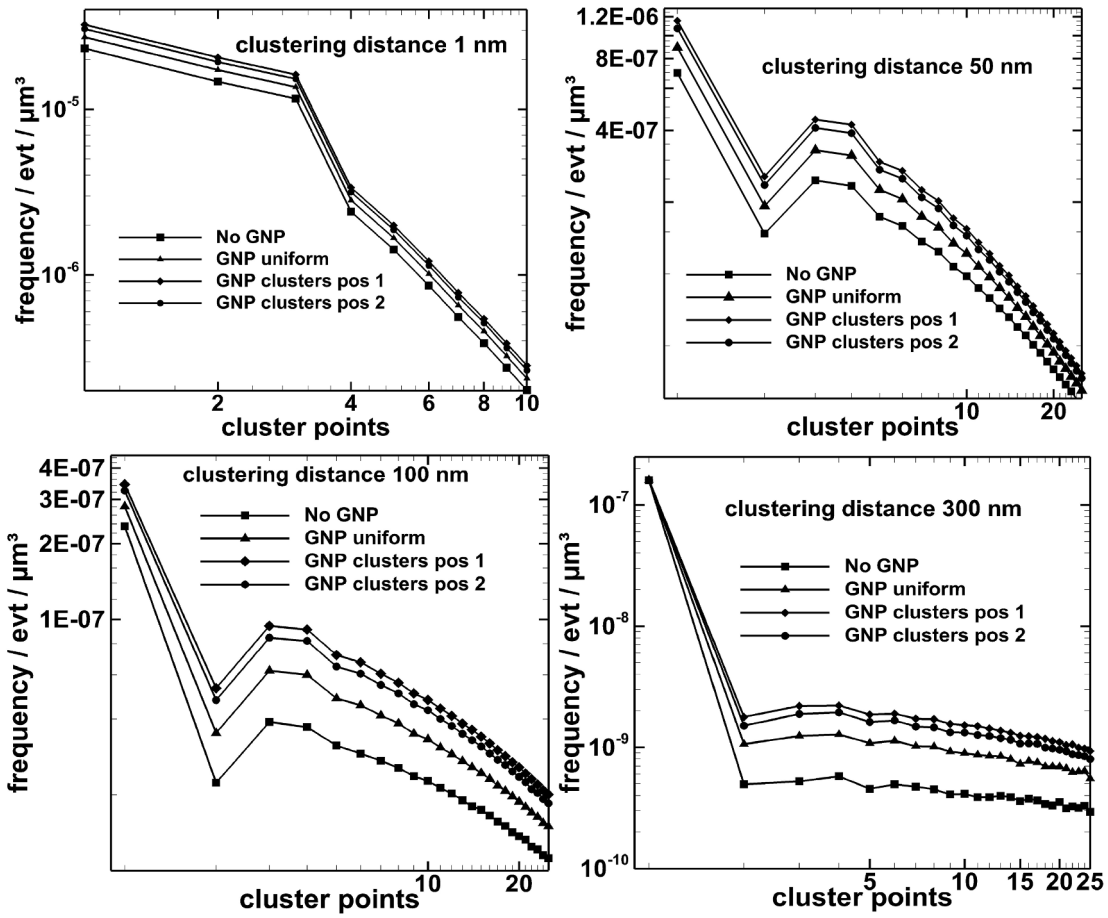

Fig. 3. Cluster size frequencies of energy depositions in the water cube (*World* volume) excluding energy depositions in the mitochondrial tube. Results are shown for different clustering maximum distances (1 nm, 50 nm, 100 nm and 300 nm) and different nanoparticles distributions; uniform distribution noted "GNP uniform", clusters of vesicles distributions noted "GNP clusters pos 1" and "GNP clusters pos 2". For comparison, the results obtained without nanoparticles are also shown ("No GNP").

of occurrence is displayed versus the cluster size, expressed in number of points contained within the cluster. The resulting distributions are then normalized as previously mentioned in this section. The results are shown for 4 different geometry configurations; the first containing no GNP as noted on the figure, the second geometry contains GNPs uniformly distributed in the water cube (noted "GNP uniform"), the third and fourth contain GNPs in clusters of vesicles and the clusters were positioned randomly in two different configurations but without overlapping (noted "GNP clusters pos 1" and "GNP clusters pos 2" respectively). The uncertainties on frequencies are dependent on the clustering distance; they increase for higher distances since the total number of clusters decreases. Uncertainties for values displayed in Fig. 3 are less than 3% for distances 1 nm, 50 nm and 100 nm, they reach a maximum of 6% for 300 nm clustering distance.

More random positions of GNP clusters were investigated showing that the results are highly dependent on their positioning, for clarity we will only show two positions as an example. Naturally, the GNP clusters would yield a higher energy deposition effect when centered and aligned within the beam due to a higher geometrical cross section but also if they are positioned closer to the center where all the energy depositions are considered for clustering. For GNP clusters positioned on the boundary of the simulation cube a part of the induced energy depositions is carried outside the water cube (*World* volume) and ignored, hence a lower observed effect as shown in Fig. 3. In reality, we also expect that GNPs positioned at the boundary of a cell would have less effect than those in the center. However, even boundary positioned GNPs can have an important biological effect on the cell membrane. In any clustered vesicles configuration, the calculated effect was higher than the uniform distribution and this is seen in the example represented in Fig. 3 by comparing the curves labeled "GNP uniform" and "GNP clusters".

Fig. 4 shows the same comparison as Fig. 3 for energy depositions inside the *mitochondrial tube*. The same behavior is seen where the lowest energy deposition frequencies are observed when no GNP are included, and the clustered geometry setups have more enhancement effect than the uniform GNP distribution geometry. Uncertainty values where less than 8% for 1 nm and 50 nm distances and reached a maximum of 10% for 100 nm. For 300 nm, the results reveal low statistical quality with up to 45% uncertainty, therefore they are only included to show the general trend of the frequencies distribution. In fact, it was very difficult to obtain better results even for higher numbers of simulation events, mainly because the clustering *maximum distance* is almost equal to the diameter of the *mitochondrial tube* itself and initially the number of interactions scored inside the *tube* is relatively low due to its small dimensions. Therefore, using a high clustering distance would lead to a very low total number of energy clusters for each event and this is directly related to high uncertainties.

Results represented in both Figs. 3 and 4 show that the clustering *maximum distance* parameter affects the shape of the frequency distribution. Low distances, e.g., 1 nm, show a decreasing distribution for cluster sizes between 1 and 10 points and this trend also continues for higher cluster sizes although not shown on all the figures for clarity reasons. The general effect of higher clustering *maximum distances*, e.g., 50 nm and 100 nm, is clear on Fig. 3 where there is a decrease in

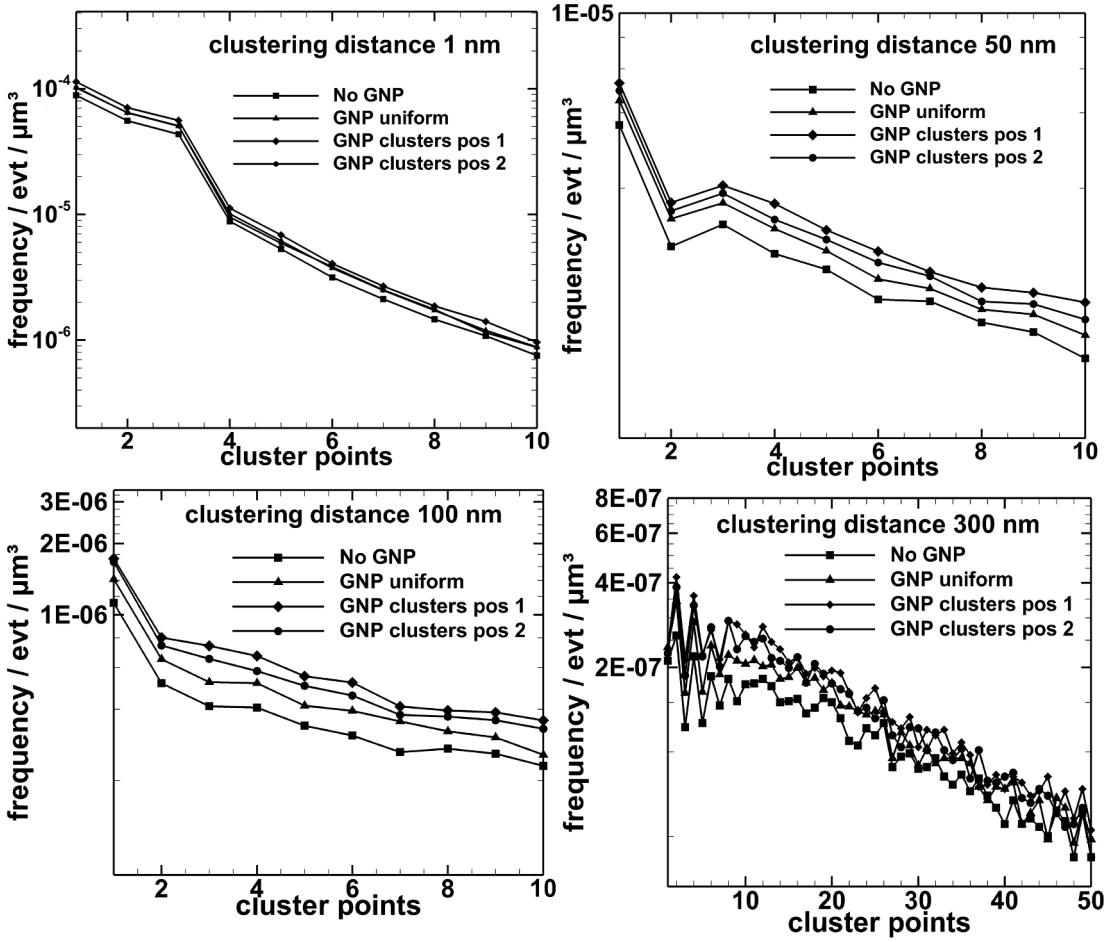

Fig. 4. Cluster size frequencies of energy depositions in the tube for different clustering distances (1 nm, 50 nm, 100 nm and 300 nm) and different nanoparticles distributions, the legend is the same as for Fig. 3.

clusters of 2 points and relatively higher frequencies for clusters of 3 and 4 points while higher size clusters exhibit a continuous decrease in frequencies. For clustering *maximum distances* above 300 nm the peak observed for 3 and 4 points clusters disappears mainly because these are merged with other clusters to form larger size clusters, hence the slow decreasing distribution observed in the bottom right part of Fig. 3. These descriptions are not clearly shown by Fig. 4 because they are limited by the size of the *mitochondrial tube*, however differences can still be noted between the different clustering distances and for the different GNP distributions.

The enhancement ratios were calculated by dividing the integrated frequencies of energy clusters for the different geometry configurations over the integrated frequencies obtained for water without GNP. This ensures that the obtained ratio is an average value considering all sizes of energy clusters. The results obtained in the water cube volume and the central tube are represented in Figs. 5 and 6 respectively versus the clustering distance.

The energy depositions in both scoring volume; the water cube (*World* volume) and the contained *mitochondrial tube*, were calculated and the dose enhancement ratios were obtained by dividing the dose for each geometry configuration by the configuration where only water was used without GNPs.

Tables 1 and 2 show the dose and enhancement ratio in the water cube and the mitochondrial tube respectively, for different geometry configurations. These numbers are introduced in order to assess whether any difference can be observed between comparing the total energy deposition values and the nanometric scale energy deposition clustering.

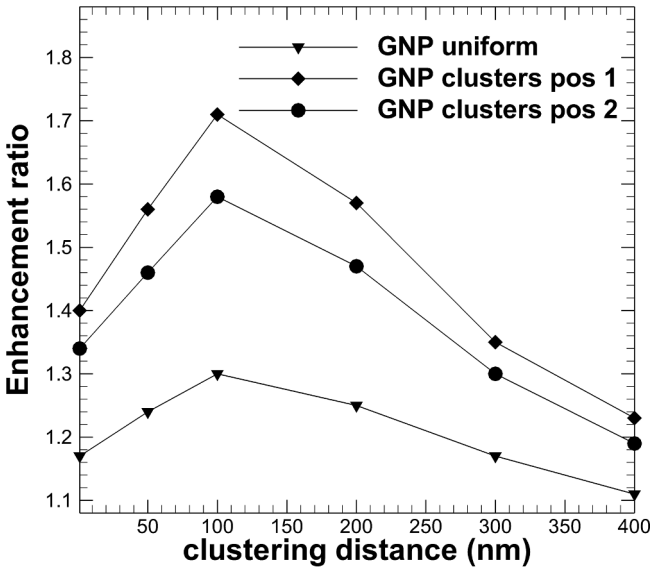

Fig. 5. Enhancement ratios obtained from energy depositions clusters in the water cube (World volume) versus clustering maximum distance for the 3 geometry configurations.

For small clustering *maximum distances*, e.g., 1 nm, the enhancement ratios obtained from clusters in both scoring volumes are comparable to the ratios obtained from dose calculations showing no advantage of the clustering procedure. Enhancement ratios start to show noticeable

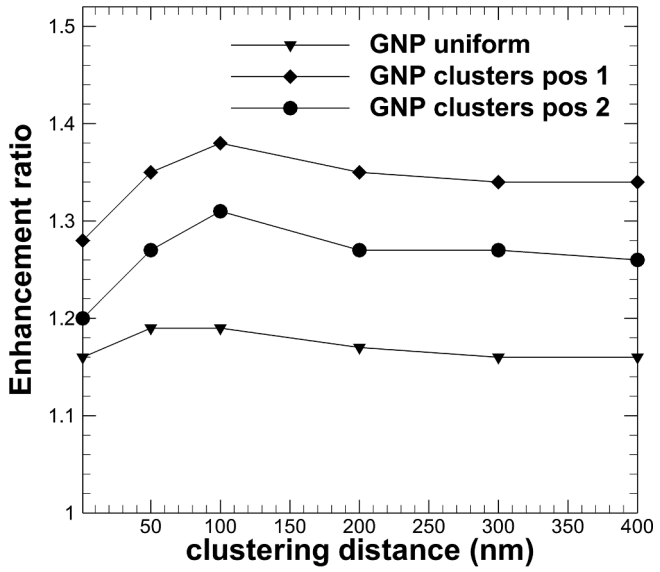

Fig. 6. Enhancement ratios from energy clustering in the mitochondrial tube versus clustering maximum distance for the 3 geometry configurations.

Table 1
Dose deposition and enhancement ratios in the water cube (World volume).

Geometry configuration	Energy deposition [eV/evt]	Energy deposition uncertainty	Enhancement ratio
No GNP	1.14	0.07%	–
GNP Uniform	1.34	0.10%	1.17
GNP clusters pos 1	1.59	0.03%	1.39
GNP clusters pos 2	1.51	0.11%	1.32

Table 2
Dose deposition and enhancement ratios in the central mitochondrial tube.

Geometry configuration	Energy deposition [eV/evt]	Energy deposition uncertainty	Enhancement ratio
No GNP	0.0015	0.58%	–
GNP Uniform	0.0017	2.56%	1.13
GNP clusters pos 1	0.0019	0.72%	1.26
GNP clusters pos 2	0.0018	1.85%	1.2

differences for larger clustering distances reaching a peak of 1.7 for clustered GNP distribution at 100 nm as seen in Fig. 5. The decrease seen in Fig. 5 is attributed to the merging of clusters for such high distance thus decreasing the absolute total number of clusters. In other words, taking the extreme case of an infinite clustering *maximum distance* leads to an average of one single cluster per event in any irradiation simulation and therefore to an enhancement ratio also equal of 1. Therefore, all ratios will decrease back to unity with the increasing clustering *maximum distance*.

The enhancement ratios shown in Fig. 6 for the *mitochondrial tube* clusters show the same increase as in Fig. 5 up to 100 nm, followed by a slight decrease for higher distances.

4. Conclusion

In this work Monte-Carlo simulations were carried out using Geant4 with the Livermore and the Geant4-DNA processes to assess the effects of gold nanoparticles as radiation enhancers in a water like medium. In order to show the effect of spatial distribution of GNPs on enhancement ratios, 4 different configurations were simulated including one where no GNPs were considered. The DBSCAN clustering algorithm was used to analyze energy deposition patterns using different clustering distances.

The results showed a clear enhancement effect on the dose and the number of clusters when GNP were included in the calculations. However, a higher ratio was noticed for the number of clusters especially for the clustered GNP configurations reaching a factor of 1.7 for a maximum clustering distance of 100 nm.

The enhancement ratios were noticeably different for the different GNP distributions showing that clusters of vesicles containing GNPs are more efficient than uniformly distributed GNPs. Therefore it is possible to achieve high enhancement ratios if the configuration observed by Peckys and de Jonge [14] is applicable to all types of cells. Our results show the importance of information about nanoparticles uptake in the cell and their exact distribution within the cell volume especially when considering sensitive structures such as the nucleus and mitochondrial DNA or the mitochondrial volume itself. However, in order to draw a firm conclusion on nanoparticles uptake and distributions more experimental data is needed taking into consideration different cell types, different nanoparticles dimensions and different GNP coating.

Increasing the clustering maximum distances revealed higher enhancement ratios, this is an important indicator that taking into account electron thermalization and free radicals diffusion would have an impact on the results. In this study electrons were stopped at 9 eV and it is possible for such electrons to spread their energy over a track of few tens of nanometers which is being ignored in our simulations. Moreover, free radicals can also diffuse by few nanometers and these distances can affect enhancement ratios and biological effects for example when looking at DNA damage.However, it is not possible to estimate a prediction of these effects without a detailed simulation, since the geometrical configuration can play a complicated role. For example clusters of GNPs would generate local high densities of free radicals that might have a high recombination yields among each other and the outcome can only be estimated with adequate processes.

5. Acknowledgements

Z. Francis would like to thank the Research Council of the Saint Joseph University for supporting this study under the projects FS133 and FS-SF1. M. A. Bernal would like to thank the Conselho Nacional para o Desenvolvimento Científico e Tecnológico (CNPq), Brazil, for financing his research activities through the project 306775/2015-8. He also acknowledges the support received from the FAPESP foundation in Brazil, through the 2011/51594-2, 2015/21873-8, and 2018/15316-7 projects.

References

[1] Mello RS, Callisen H, Winter J, Kagan AR, Norman A. Radiation dose enhancement in tumors with iodine. Med Phys 1983;10(1):75–8.
[2] Matsudaira H, Ueno A, Furuno I. Iodine contrast medium sensitizes cultured mammalian cells to x rays but not to gamma rays. Rad Res 1980;84(1):144–8.
[3] Iwamoto KS, Cochran ST, Winter J, Holburt E, Higashida RT, Norman A. Radiation dose enhancement therapy with iodine in rabbit vx–2 brain tumors. Radiother Oncol 1987;8(2):161–70.
[4] Mesa AV, Norman A, Solberg TD, Demarco JJ, Smathers JB. Dose distributions using kilovoltage x-rays and dose enhancement from iodine contrast agents. Phys Med Biol 1999;44(8):1955–68.
[5] Wang L, Li Q, Wang X-M, Hao G-Y, Jie-Bao SHu, et al. Enhanced radiation damage caused by iodinated contrast agents during ct examination. Eur J Radiol 2017;92:72–7.
[6] Hyun Cho S. Estimation of tumour dose enhancement due to gold nanoparticles during typical radiation treatments: a preliminary monte carlo study. Phys Med Biol 2005;50:N163–73.
[7] Lechtman E, Mashouf S, Chattopadhyay N, Keller BM, Lai P, Cai Z, et al. A monte carlo-based model of gold nanoparticle radiosensitization accounting for increased radiobiological effectiveness. Phys Med Biol 2013;58:3075–87.
[8] Kraft G, Scholz M, Bechthold U. Tumor therapy and track structure. Rad Environ Biophys 2000;38:229–37.
[9] Carter J, Cheng N, Qu Y, Suarez G, Guo T. Nanoscale energy deposition by x-ray absorbing nanostructures. J Phys Chem B 2007;111:11622–5.

[10] McMahon SJ, McNamara AL, Schuemann J, Prise KM, Paganetti H. Mitochondria as a target for radiosensitisation by gold nanoparticles. J Phys: Conf Ser 2017;777:012008.
[11] Estaquier J, Vallette F, Vayssiere J, Mignotte B. The mitochondrial pathways of apoptosis. Adv Exp Med Biol 2012;942:157–83.
[12] Zhou X, Li N, Wang Y, Wang Y, Zhang X, Zhang H. Effects of x-irradiation on mitochondrial dna damage and its supercoiling formation change. Mitochondrion 2011;11(6):886–92.
[13] Karataş Ömer Faruk, Sezgin E, Ömer AydínÇulha M. Interaction of gold nanoparticles with mitochondria. Colloids Surf B 2009;71(2):315–8.
[14] Peckys D, Jonge N. Visualizing gold nanoparticle uptake in live cells with liquid scanning transmission electron microscopy. Nano Lett 2011;11:1733–8.
[15] Kirkby C, Ghasroddashti E. Targeting mitochondria in cancer cells using gold nanoparticle-enhanced radiotherapy: a Monte Carlo study. Med Phys 2015;42(2):1119–28.
[16] Peckys DB, de Jonge N. Gold nanoparticle uptake in whole cells in liquid examined by environmental scanning electron microscopy. Microsc Microanal 2014;20(1):189–97.
[17] Jeynes JCG, Jeynes C, Merchant MJ, Kirkby KJ. Measuring and modelling cell-to-cell variation in uptake of gold nanoparticles. Analyst 2013;138:7070–4.
[18] Ester M, Kriegel H-P, Sander J, Xu X. A density-based algorithm for discovering clusters a density-based algorithm for discovering clusters in large spatial databases with noise. Proceedings of the Second International Conference on Knowledge Discovery and Data Mining, KDD'96. AAAI Press; 1996. p. 226–31.
[19] Francis Z, Seif E, Incerti S, Champion C, Karamitros M, Bernal MA, et al. Carbon ion fragmentation effects on the nanometric level behind the bragg peak depth. Phys Med Biol 2014;59(24):7691–702.
[20] Zein S, Francis Z, Montarou G, Chandez F, Kane M, Chevrollier A. Microdosimetry in 3d realistic mitochondria phantoms: Geant4 monte carlo tracking of 250kev photons in phantoms reconstructed from microscopic images. Phys Med 2017;42:7–12.
[21] Hainfeld J, Slatkin D, Smilowitz H. The use of gold nanoparticles to enhance radiotherapy in mice. Phys Med Biol 2004;49:N309–15.
[22] Sotiropoulos M, Henthorn NT, Warmenhoven JW, Mackay RI, Kirkby KJ, Merchant MJ. Modelling direct dna damage for gold nanoparticle enhanced proton therapy. Nanoscale 2017;9:18413–22.
[23] Agostinelli S, Allison J, Amako K, Apostolakis J, Araujo H, Arce P, et al. Geant4–a simulation toolkit. Nucl Instrum Methods Phys Res Sect A 2003;506(3):250–303.
[24] Allison J, Amako K, Apostolakis J, Araujo H, Arce Dubois P, Asai M, et al. Geant4 developments and applications. IEEE Trans Nucl Sci 2006;53(1):270–8.
[25] Allison J, Amako K, Apostolakis J, Arce P, Asai M, Aso T, et al. Recent developments in geant4. Nucl Instrum Methods Phys Res Sect A 2016;835:186–225.
[26] Cullen D, Chen M, Hubbell J, Perkins S, Plechaty E, Rathkopf J, et al. Epdl: evaluated photon data library of the lawrence livermore national laboratory; 1994.
[27] Perkins S, Cullen D, Seltzer S. Eedl evaluated electron data library of the lawrence livermore national laboratory; 1994.
[28] Incerti S, Suerfu B, Xu J, Ivantchenko V, Mantero A, Brown J, et al. Simulation of auger electron emission from nanometer-size gold targets using the geant4 monte carlo simulation toolkit. Nucl Instrum Methods Phys Res Sect B 2016;372:91–101.
[29] Xie WZ, Friedland W, Li WB, Li CY, Oeh U, Qiu R, et al. Simulation on the molecular radiosensitization effect of gold nanoparticles in cells irradiated by x-rays. Phys Med Biol 2015;60(16):6195–212.
[30] Sakata D, Kyriakou I, Okada S, Tran HN, Lampe N, Guatelli S, et al. Geant4-dna track-structure simulations for gold nanoparticles: the importance of electron discrete models in nanometer volumes. Med Phys 2018;45(5):2230–42.
[31] Ashley JC, Tung CJ, Ritchie RH, Anderson VE. Calculations of mean free paths and stopping powers of low energy electrons (< 10 kev) in solids using a statistical model. IEEE Trans Nucl Sci 1976;23(6):1833–7.
[32] Incerti S, Baldacchino G, Bernal M, Capra R, Champion C, Francis Z, et al. The geant4-dna project. Int J Model Simul Scientific Comput 2010;1(2):157–78.
[33] Incerti S, Ivanchenko A, Karamitros M, Mantero A, Moretto P, Tran HN, et al. Comparison of geant4 very low energy cross section models with experimental data in water. Med Phys 2010;37(9):4692–708.
[34] Bernal M, Bordage M, Brown J, Davídková M, Delage E, Bitar ZE, et al. Track structure modeling in liquid water: a review of the geant4-dna very low energy extension of the geant4 monte carlo simulation toolkit. Physica Med 2015;31(8):861–74.
[35] Incerti S, Kyriakou I, Bernal MA, Bordage MC, Francis Z, Guatelli S, et al. Geant4-dna example applications for track structure simulations in liquid water: a report from the geant4-dna project. Med Phys 2018;45(8):e722–39.
[36] Nikjoo H, Ueharas W, Wilson E, Hoschi M, Goodhead D. Track structure in radiation biology: theory and applications. Int J Rad Biol 1998;73(4):355–64.
[37] Pszona S, Bantsar A, Nikjoo H. Ionization cluster size distribution for alpha particles: experiment, modelling. Rad Prot Dosim 2007;122(1–4):28–31.
[38] Hartigan JA. Clustering algorithms. 99th ed. New York, NY, USA: John Wiley & Sons Inc; 1975.
[39] Francis Z, Villagrasa C, Clairand I. Simulation of dna damage clustering after proton irradiation using an adapted dbscan algorithm. Comput Methods Programs Biomed 2011;101(3):265–70.
[40] Francis Z, Incerti S, Ivanchenko V, Champion C, Karamitros M, Bernal M, et al. Monte carlo simulation of energy-deposit clustering for ions of the same let in liquid water. Phys Med Biol 2011;57:209–24.